PHYSICAL REVIEW B **109**, 174408 (2024)

Scaling relation and low-temperature anomaly of the anomalous Hall effect in the Van der Waals ferromagnet Fe_3GeTe_2

Dongchao Yang[1] and S. M. Zhou[1,2,*]
[1]Shanghai Key Laboratory of Special Artificial Microstructure Materials and Technology and Pohl Institute of Solid State Physics, School of Physics Science and Engineering, Tongji University, Shanghai 200092, China
[2]School of Materials Science and Engineering, Anhui University, Hefei 230601, China

(Received 9 January 2024; accepted 10 April 2024; published 3 May 2024)

The van der Waals (vdW) ferromagnet Fe_3GeTe_2 (FGT) has recently attracted much attention due to its fruitful physical phenomena. In this paper, by varying the thickness of FGT nanoflakes, the relationship between anomalous Hall conductivity (AHC) σ_{AH} and the sheet electric conductivity σ_{xx} in FGT is found to follow $\sigma_{\mathrm{AH}} \propto \sigma_{xx}^{\gamma}$, where γ varies from 1.4 to 2.2 as the temperature increases from 2 K to the Curie temperature of 200 K. The scaling relation is found to be near the transition between the intrinsic and dirty regimes, suggesting a dual origin involving the intrinsic Berry curvature and the strong scattering. Moreover, an upturn of the sheet resistivity <20 K is caused by the electron-electron interaction due to Fe vacancies and the quantum correction to the AHC is negligible. This paper is beneficial to the further understanding of the physics of the AHC in vdW ferromagnets.

DOI: 10.1103/PhysRevB.109.174408

I. INTRODUCTION

Van der Waals (vdW) materials [1,2] feature strong intralayer but weaker interlayer bonding forces, which endows them the potential to be exfoliated layer by layer into two-dimensional (2D) structures. The fabrication of graphene via the mechanical exfoliation method and discovery of its astonishing physical properties sparked a surge of interest in 2D materials research [3,4]. To date, thousands of 2D materials have been identified [5], including metals, semimetals, superconductors, semiconductors, and insulators, which opened up opportunities to design high-performance low-dimensional devices [6].

On the other hand, whether long-range magnetic order can exist in 2D materials is a long-standing question. According to the Mermin-Wagner theory [7], 2D long-range magnetic order would be destroyed by thermal fluctuation at finite temperatures. Magnetic 2D materials CrI_3 [8], $CrGeTe_3$ [9], and Fe_3GeTe_2 (FGT) [10] were experimentally confirmed, which is attributed to their strong magnetic anisotropy energy against the thermal fluctuation. FGT exhibits a high Curie temperature ($T_c \sim 220$ K for bulk, 90 K for monolayer) compared with other identified 2D magnets, making it particularly attractive for realization of 2D devices near room temperature. Recently, the high Curie temperature 2D magnets in the FGT family have also been enriched, such as Fe_nGeTe_2 [11] ($3 < n < 5$, 200–400 K) and Fe_3GaTe_2 [12] (367 K). Additionally, fruitful physical properties have been found in FGT, including large perpendicular anisotropy, heavy fermion behavior, Kondo lattice, and topological nodal lines [13–15].

The unified theory and extensive experiments of various magnets indicate that the scaling behavior of the anomalous Hall effect (AHE) can be divided into three regimes [16,17]: (i) a superclean metallic regime with high conductivity ($\sigma_{xx} \gtrsim 10^6$ S/cm), in which $\sigma_{\mathrm{AH}} \propto \sigma_{xx}$ due to the dominant role of the skew scattering; (ii) in the moderate dirty regime ($10^4 \lesssim \sigma_{xx} \lesssim 10^6$ S/cm), the intrinsic mechanism and side jump contribute to AHE, where σ_{AH} is nearly a constant and independent of σ_{xx}; and (iii) a dirty regime ($\sigma_{xx} \lesssim 10^4$ S/cm) in which $\sigma_{\mathrm{AH}} \propto \sigma_{xx}^{\gamma}$, where one generally has [18] $\gamma \sim 1.6$. It is noteworthy that the quantum corrections to the scaling relation, due to electron-electron Coulomb interaction (EEI) or weak localization in disordered films and strongly correlated electrons in heavy fermion systems, have not been considered in the unified theory [19–21]. These quantum corrections to the AHE are still an open issue. For example, in ultrathin CNi_3 and FePt films, the value of γ changes from 1.6 for weak disordered films to 2.0 for highly disordered films, which was interpreted as the weak localization-induced correction to σ_{AH} [20,22]. Siddiquee *et al.* [23] reported the breakdown of the scaling relation of the AHE in heavy fermion material USbTe. VdW material $CrTe_2$ [24] was reported to exhibit colossal anomalous Hall conductivity (AHC), deviating from the theoretical scaling curve. Therefore, it is necessary to investigate the scaling law of the AHE in new materials, particularly in 2D vdW ferromagnetic materials, to deeply understand the unified theory of the AHE.

In this paper, the scaling relation of the AHE in vdW material FGT nanoflakes was studied by varying both the nanoflake thickness (t) and the temperature. It was found that FGT nanoflakes show bad electric conductivities due to Fe vacancies and heavy fermion characteristics, leading to the scaling relation of the AHE falling into the transition region between the intrinsic and dirty regimes. Therefore, in addition to the Berry curvature, the strong scattering also greatly influences the scaling relation of the AHE. Moreover, we observed low-temperature anomalies of the longitudinal and anomalous

---

[*] shiming@tongji.edu.cn

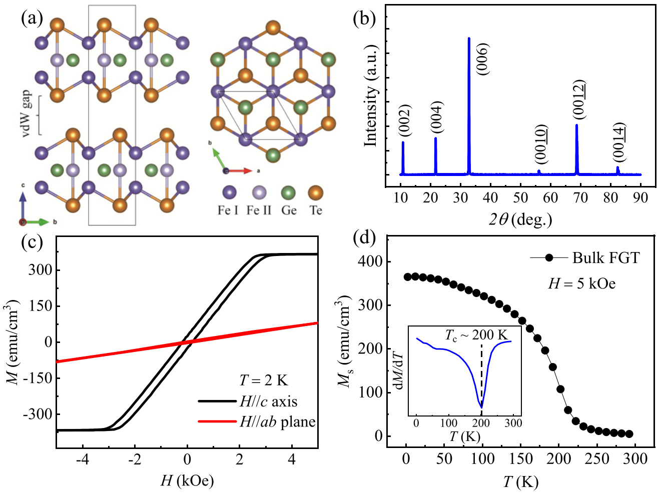

FIG. 1. Crystal structure and magnetic properties of bulk FGT. (a) Crystal structure (side view and top view) of FGT with a van der Waals (vdW) gap of 2.95 Å. Inequivalent Fe sites are labeled I and II, respectively. Solid frames represent the unit cell of FGT. (b) X-ray diffraction (XRD) pattern for the pristine FGT single crystal. (c) Hysteresis loops of bulk FGT measured along the *ab* plane and the *c* axis at 2 K. (d) Temperature dependence of saturation magnetization M_s. Inset: dM/dT determines the Curie temperature of $T_c \sim 200$ K.

Hall resistivities, which was interpreted as three-dimensional (3D) enhanced EEI.

II. SAMPLE FABRICATION AND MEASUREMENTS

Single-crystal FGT was synthesized by the chemical vapor transport method, as described in our previous work [25]. To prepare FGT nanoflakes for the electrical transport measurements, the mechanical exfoliation method was adopted. An FGT single crystal was exfoliated with Scotch tape and transferred onto a 280 nm SiO_2/Si substrate. The entire transfer process was conducted within the glove box to avoid FGT degradation caused by O_2 and H_2O in ambient conditions. Then the ultraviolet lithography process was utilized to fabricate electrodes. Here, Ta(2 nm)/Au(50 nm) electrodes were deposited by magnetron sputtering. Afterward, the devices were immediately transferred to the vacuum chamber of the Physical Property Measurement System (PPMS, Quantum Design) for electrical transport measurements. Four electrodes were utilized for electrical characterization by a van der Pauw method. The Hall resistivity was measured under an out-of-plane magnetic field. After completing the electrical transport measurements, the thickness of FGT nanoflakes was confirmed by atomic force microscope (AFM, Bruker Dimension Edge). The crystal quality of bulk FGT was characterized by x-ray diffraction (XRD, Bruker D8) with Cu $K\alpha(\lambda = 0.15419\,\text{nm})$. The element analysis was performed using energy-dispersive x-ray spectroscopy (EDX).

III. RESULTS AND DISCUSSION

A. Structural and magnetic properties of FGT

As shown in Fig. 1(a), a hexagonal FGT monolayer contains five atomic layers stacked with a Te-Fe-GeTe-Fe-Te sequence. The adjacent FGT monolayers are bounded through weak vdW force with a vdW gap of ~2.96 Å. The Fe atoms occupy two inequivalent Wyckoff positions denoted as Fe I and Fe II, corresponding to Fe^{3+} and Fe^{2+} ions [26]. The $(0\,0\,2n)$ diffraction peaks in Fig. 1(b) indicate the high quality and the orientation of the pristine FGT. The lattice parameter is determined to be $c = 16.3817 \pm 0.0068$ Å. The hysteresis loop of single-crystal FGT in Fig. 1(c) shows a perpendicular magnetic anisotropy along the *c* axis. The saturation magnetization is measured to be $M_s = 365$ emu/cm^3 (i.e., 1.50 μ_B/Fe) at 2 K, in agreement with theoretical calculations predicting an average magnetic moment of 1.48 μ_B per Fe atom [27]. The temperature-dependent magnetization shows that the Curie temperature T_c is 200 K, as shown in Fig. 1(d). It has been reported that, in Fe_xGeTe_2, the Curie temperature T_c varies from 140 to 230 K, and the lattice parameter *c* varies from 16.32 to 16.41 Å, when $2.7 < x < 3.1$ [15]. In this paper, the precise atomic ratio is determined by EDX to be $Fe_{2.87}Ge_1Te_{2.14}$. Accordingly, the preparation of single-crystal FGT unavoidably introduces Fe vacancies.

B. Scaling relation of AHE in FGT

As shown in Fig. 2(a), exfoliated FGT nanoflakes were patterned into four electrodes for the van der Pauw method. To investigate the scaling relation of the AHE, the thickness of FGT nanoflakes was measured by AFM, as shown in Fig. 2(b). In the present experiments, the thickness of FGT nanoflakes changes from 11 to 90 (nm), and thus, the longitudinal resistivity changes from ~800 to ~200 (μΩ cm), much larger than that of conventional ferromagnetic metallic films of Fe, Co, and Ni, $\rho \sim 50$ μΩ cm. According to the Drude model, i.e., $\rho_{xx} = m^*/(ne^2\tau)$, the effective mass ($m^*$) of electrons in FGT is much larger than that of free electrons (m). Indeed, the heavy fermion behavior and $m^*/m = 15.9$ in FGT have been identified by the specific heat measurements [25]. The presence of Fe vacancies is another factor contributing to the relatively high resistivity of FGT.

The linear dependence of resistivity on the inverse layer thickness $1/t$ in Fig. 2(c) indicates the surface scattering contribution to the resistivity [28]. Figure 2(d) shows the ratio $\rho_{xx}(T)/\rho_{xx}(300\,\text{K})$ for different thicknesses. The sudden turn of ρ_{xx} near T_c indicates that the magnetic scattering is saturated above the Curie temperature. At temperatures <20 K, the resistivity exhibits an anomaly upturn behavior, which can be ascribed to the disorder-induced EEI, as discussed below. Since the ratio $\rho_{xx}(2\,\text{K})/\rho_{xx}(300\,\text{K})$ is ~0.9, the temperature-dependent ρ_{xx} is close to the transition from metallic to insulating regimes. In fact, an insulating behavior, characterized by an increasing in resistivity as decreasing temperature, has been reported for few-layer-thick FGT [10,29].

As shown in Fig. 2(e), the transverse resistance was measured by sweeping the out-of-plane magnetic field at temperatures from 2 to 200 K, and the anomalous Hall resistivity ρ_{AH} at each temperature is obtained by the extrapolation from high fields to zero field. Figure 2(f) shows that, for specific thicknesses of FGT nanoflakes, the normalized Hall resistivity $\rho_{AH}/\rho_{AH}(200\,\text{K})$ decreases with increasing temperature. Like ρ_{xx}, ρ_{AH} also exhibits an upturn behavior at low temperatures. Moreover, at specific

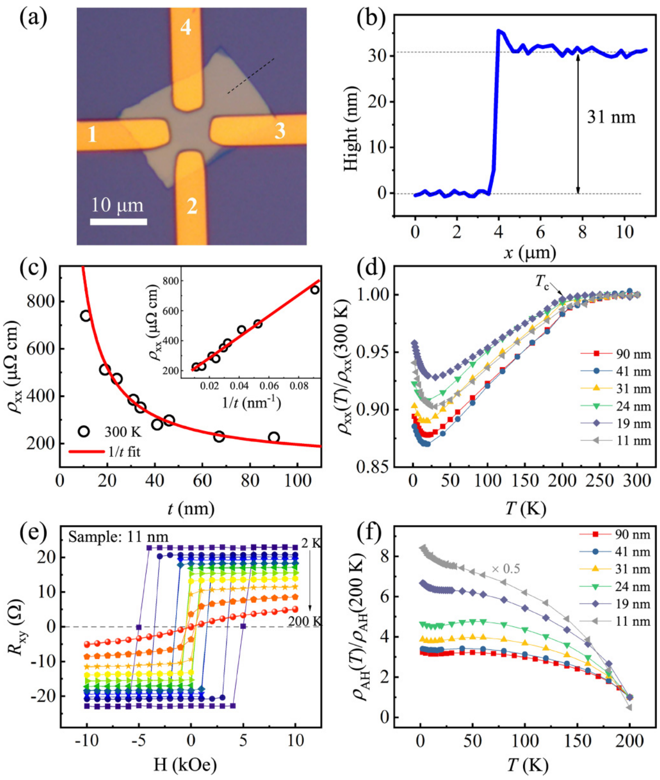

FIG. 2. Electrical transport properties of FGT nanoflakes. (a) Optical image of exfoliated 31 nm FGT nanoflake; four electrodes were prepared for electrical measurements. (b) The nanoflake thickness measured by atomic force microscopy (AFM) along the dotted line in (a). (c) The measured resistivity ρ_{xx} at 300 K as a function of FGT thickness t. Inset: A linear dependence of ρ_{xx} on $1/t$; the red lines refer to the fitted results. The temperature dependence of (d) normalized longitudinal resistivity $\rho_{xx}/\rho_{xx}(300\text{ K})$ and (f) normalized anomalous Hall resistivity $\rho_{AH}/\rho_{AH}(200\text{ K})$ for various thickness of FGT nanoflakes. (e) The Hall resistance R_{xy} as a function of the magnetic field at various temperatures for 11 nm FGT.

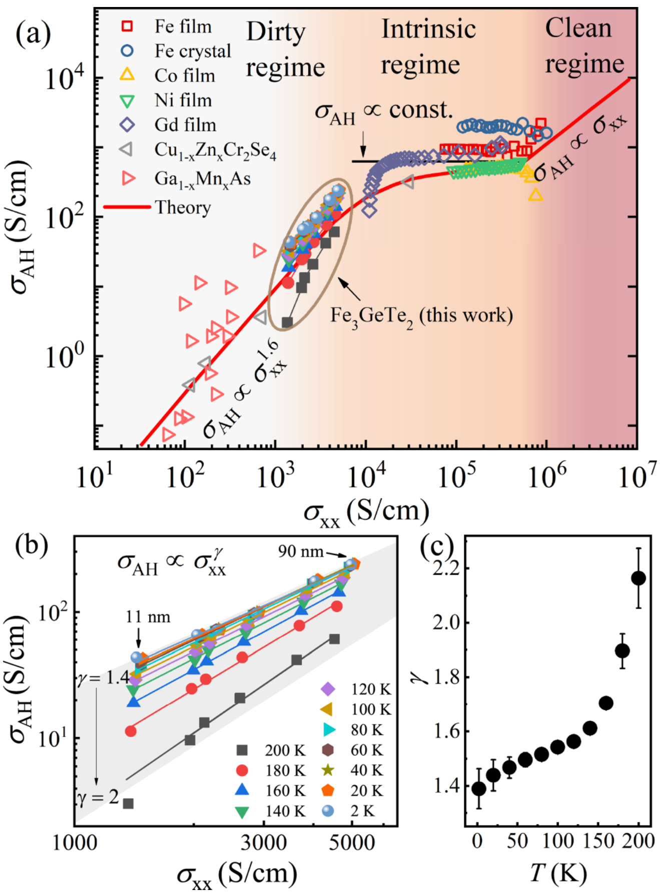

FIG. 3. Scaling relation of the anomalous Hall effect (AHE) in FGT nanoflakes. (a) Comparison between theoretical scaling relation and experimental results for various ferromagnets. The solid line represents the theoretical prediction. The FGT results in this paper are also added. The data of other ferromagnets were taken from Refs. [18,30]. (b) The scaling relation of FGT at different temperatures. The gray area represents $1.4 \leqslant \gamma \leqslant 2.2$. The inset numbers refer to the measuring temperatures. (c) With the scaling relation $\sigma_{xx} \propto \sigma_{\mathrm{AH}}^{\gamma}$, the scaling factor γ changes from 1.4 to 2.2 as the temperature increases from 2 to 200 K.

temperatures, $\rho_{\mathrm{AH}}/\rho_{\mathrm{AH}}(200\text{ K})$ decreases when the thickness of FGT nanoflakes increases.

To reveal the scaling relation of the AHE in the FGT, we plotted the AHC σ_{AH} vs the longitudinal conductivity σ_{xx} in the logarithmic coordinate system by varying the thickness of FGT nanoflakes, at specific temperatures, as shown in Fig. 3(a). For comparison, the measured and calculated AHE data of various ferromagnets are also given [18,30]. Three different regimes in Fig. 3(a) represent different mechanisms of the AHE. The scaling relation of the FGT is near the transition from the intrinsic and the dirty regimes, indicating two origins of the AHE in FGT. The first one comes from the intrinsic mechanism, where the topological nodal line near the Fermi surface contributes a large Berry curvature, as reported previously [15,31].

The second one arises from the heavy fermion characteristics [25] and/or strong scattering induced by Fe vacancies [17], i.e., $lk_F \leqslant 1.0$, with the Fermi wavevector k_F and the mean free path l. The intrinsic Berry curvature may be modified by the second mechanism [32]. As shown in Fig. 3(a), the data of FGT approximately obey the theoretical scaling relation [17], $\sigma_{\mathrm{AH}} \propto \sigma_{xx}^{1.6}$.

For clarity, Fig. 3(b) shows the zoom-in version of the data of the FGT in Fig. 3(a). The AHC shows the scaling relation $\sigma_{\mathrm{AH}} \propto \sigma_{xx}^{\gamma}$, with $1.4 \leqslant \gamma \leqslant 2.2$, except for the data at 200 K. This minor derivation at 200 K can be attributed to the fact that the Curie temperature T_c slightly decreases when the FGT nanoflake thickness $t \leqslant 20$ nm [13]. Figure 3(c) reveals that γ slightly increases from 1.4 to 1.6 <150 K, while γ sharply increases to 2.2 when the temperature T approaches T_c. For the intrinsic origin, ideally, γ should be 1, whereas for the dirty regime, it should be 1.6. Hence, the coefficient γ range between 1.4 to 2.2 indicates more of a disordered system rather than any Berry-phase-driven AHE.

C. Low-temperature anomalies of longitudinal and anomalous Hall resistivities

We now turn our attention to the electrical transport anomalies at low temperatures. When $T < 20$ K, all FGT samples exhibit an upturn in both ρ_{xx} and ρ_{AH}. Although the low-temperature anomaly in ρ_{xx} may come from the Kondo

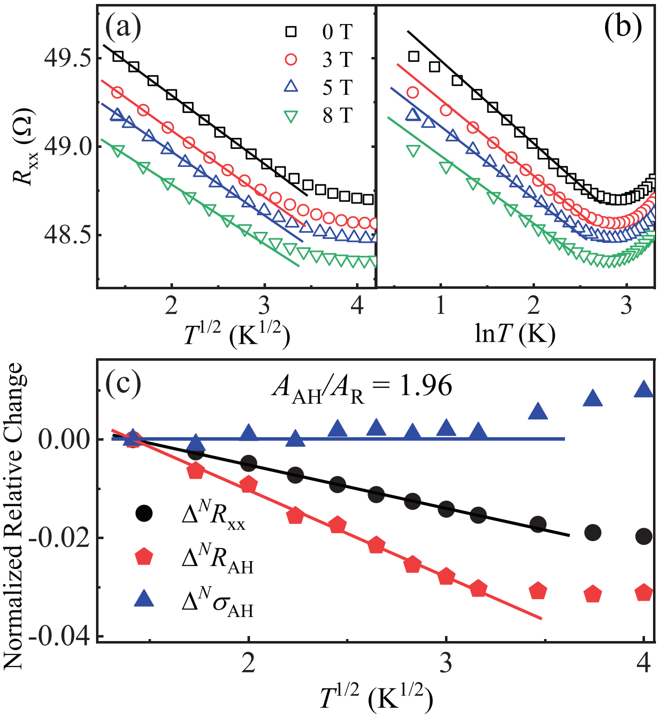

FIG. 4. Quantum correction of the electron-electron Coulomb interaction (EEI) to the anomalous Hall effect (AHE) at low temperatures. For 44-nm-thick pristine FGT nanoflakes, the sheet resistance R_{xx} vs (a) $T^{1/2}$ and (b) ln T under various out-of-plane magnetic field H_z. The solid lines serve as a guide to the eye. (c) $T^{1/2}$ dependence of normalized relative change $\Delta^N R_{xx}$, $\Delta^N R_{\mathrm{AH}}$, and $\Delta^N \sigma_{\mathrm{AH}}$ for the 40-nm-thick pristine FGT nanoflake; solid lines refer to the fitted results.

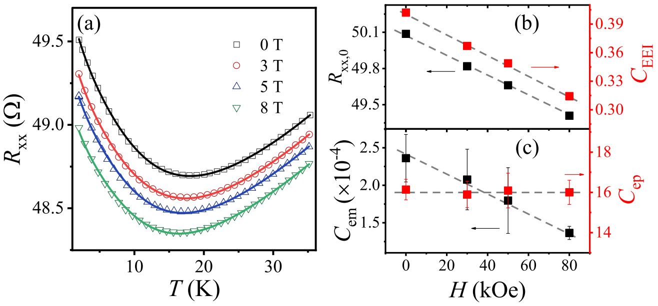

FIG. 5. Low-temperature anomaly of longitudinal resistance for a 44-nm-thick FGT nanoflake. (a) Fitting to the $R(T)$ curve using Eq. (3). Magnetic field dependencies of the fitted coefficients (b) $R_{xx,0}$ and C_{EEI} and (c) C_{em} and C_{ep}; dashed lines serve a guide to the eye. The inset numbers in (a) refer to the out-of plane magnetic field.

effect, weak localization, and EEI, we can clarify the possible mechanism of the anomaly of the electric resistivity at low temperatures, as analyzed as follows.

Firstly, the Kondo effect, often observed in dilute magnetic metallic alloys, is characterized by a minimum resistivity at low temperatures [33]. The prominent feature of the Kondo effect is that the ln$T$ dependence of resistivity and the resistivity upturn behavior can be suppressed by amagnetic field [34]. However, as shown in Fig. 4(a), the resistivity upturn in FGT cannot be suppressed even under a strong magnetic field up to 8 T. The 1% shift in resistance under a magnetic field arises from the magnetoresistance effect of FGT. Therefore, the Kondo effect can be ruled out.

Secondly, weak localization may occur in disordered electron systems, and it is characterized by a linear dependence of $\delta R_{xx}/R_{xx}$ on ln$T$ or $T^{\pm 1/2}$ at low temperatures, depending on the dimensionality of the systems [35]. Although the resistance in FGT also follows a linear dependence on $T^{1/2}$, as shown in Fig. 4(a), this mechanism can also be excluded in explanations of the anomaly of the sheet resistivity at low temperatures. This is because there is no quantum correction of the weak localization to the AHC in the FGT, as discussed below.

To identify the mechanism of the electric resistivity anomaly at low temperature, we then focus on the quantum correction of 3D-enhanced EEI to the AHE <20 K. It is theoretically predicted that the disorder-induced EEI can also lead to the following quantum correction to resistivity, i.e., $R_{xx}^{\mathrm{EEI}} \propto -\ln T$ in 2D systems and $R_{xx}^{\mathrm{EEI}} \propto -T^{1/2}$ in 3D systems [36]. Figures 4(a) and 4(b) clearly show that, for the FGT, $R_{xx}^{\mathrm{EEI}} \propto -T^{1/2}$, and the EEI in a 3D system can better explain the anomaly of the electric resistivity at low temperatures [36], when the FGT nanoflake thickness is >10 nm.

Assuming that Q refers to the sheet resistance R_{xx}, the anomalous Hall resistivity R_{AH}, the electric conductance σ_{xx}, and the anomalous Hall conductance σ_{AH}, the normalized relative change is defined as $\Delta^N Q = \delta Q/Q$, where $\delta Q = Q(T) - Q(T_0)$ and $T_0 = 2$ K here. In FGT at low temperatures, as shown in Fig. 4(a), $\Delta^N R_{xy}$ scales as a linear function of $T^{1/2}$, like the anomaly observed in $\Delta^N R_{xx}$. Defining the coefficients A_R and A_{AH} by [20,37,38]

$$\Delta^N R_{xx} = -A_R\sqrt{\frac{T}{T_0}}; \quad \Delta^N R_{\mathrm{AH}} = -A_{\mathrm{AH}}\sqrt{\frac{T}{T_0}}. \tag{1}$$

For $R_{\mathrm{AH}} \ll R_{xx}$ and using $\sigma_{xx} \propto 1/R_{xx}$, $\sigma_{\mathrm{AH}} \propto R_{\mathrm{AH}}/R_{xx}^2$, we deduce

$$\Delta^N \sigma_{xx} = A_R\sqrt{\frac{T}{T_0}}; \quad \Delta^N \sigma_{\mathrm{AH}} = (2A_R - A_{\mathrm{AH}})\sqrt{\frac{T}{T_0}}. \tag{2}$$

It is theoretically predicted that the EEI correction to the AHE satisfies the relation $A_{\mathrm{AH}} = 2A_R$. Accordingly, σ_{AH} does not change due to EEI [39], i.e., $\delta\sigma_{\mathrm{AH}}^{\mathrm{EEI}} = 0$. In experiments, A_{AH}/A_R is ~2.0, and $\Delta^N \sigma_{\mathrm{AH}} \sim 0$ when the FGT thickness changes from 11 to 90 nm. Accordingly, $\Delta^N \sigma_{\mathrm{AH}}$ at low temperatures changes little with temperature, as proved by typical results of 40-nm-thick FGT nanoflakes in Fig. 4(c). Similar results are observed in amorphous Fe films [38]. Apparently, the upturn of the sheet resistivity at low temperatures mainly arises from the EEI, instead of the weak localization. This is because the quantum correction of the weak localization to the AHC from the skew scattering cannot be neglected [40].

The temperature-dependent resistance in Fig. 5(a) can be described by [41,42]

$$R_{xx}(T) = R_{xx,0} - C_{\mathrm{EEI}}T^{1/2} + C_{em}T^2 + C_{ep}\left(\frac{T}{\Theta_D}\right)^5 \times \int_0^{\Theta_D/T} \frac{x^5}{(e^x - 1)(1 - e^{-x})}dx, \tag{3}$$

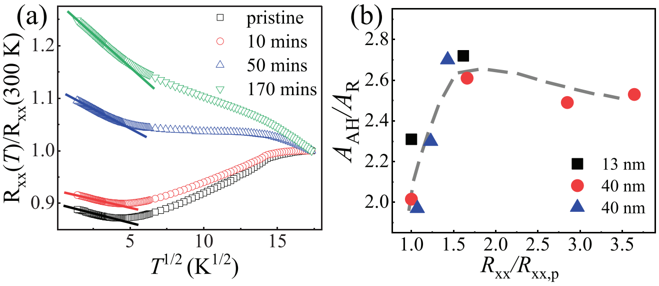

FIG. 6. (a) For 40-nm-thick FGT nanoflakes, normalized R_{xx} as a function of $T^{1/2}$ with different oxidation times. (b) A_{AH}/A_R as a function of $R_{xx}/R_{xx,p}$ at room temperature by varying oxidation time. Solid and dotted lines are guides to the eye. The inset numbers in (a) and (b) refer to the oxidization time and the FGT thickness, respectively.

where the residual resistance $R_{xx,0}$, caused by defects, is temperature independent, and the $T^{1/2}$ and T^2 terms originate from 3D-enhanced EEI and the electron-magnon scattering or the electron-electron scattering in the Fermi liquid model, respectively. The last term is associated with the electron-phonon scattering and obeys the Bloch-Grüeisen formula. The Debye temperature Θ_D of a 44-nm-thick FGT nanoflake is fitted to be 93 K, much lower than the bulk FGT value of 217 K [25]. This discrepancy is likely attributed to the influence of size effect [43]. Figures 5(b) and 5(c) summarize the fitted coefficients as a function of the magnetic field. The decrease in $R_{xx,0}$ with increasing H can be attributed to the magnetoresistance effect in FGT. Moreover, it is well known that the disorder-induced EEI and the electron phonon scattering should not be affected by the magnetic field H. Accordingly, the coefficient C_{ep} is independent of H. While C_{EEI} is also expected to be independent of H, we observe a magnetic field-induced alteration $|\delta C_{\mathrm{EEI}}| = \left|\frac{C_{\mathrm{EEI}}(H=8T)-C_{\mathrm{EEI}}(H=0T)}{C_{\mathrm{EEI}}(H=0T)}\right| \sim 18\%$, a magnitude consistent with the previous report [44]. In combination with the $-T^{1/2}$ dependence of resistance in Fig. 4(a) and absence of quantum corrections to AHE observed in Fig. 4(c), the 3D-enhanced EEI is suggested to account for the low-temperature anomaly in resistance. Finally, the spin-wave gap in the spin-wave spectrum is proportional to $g\mu_B H$, resulting in reductions of both the number of magnons and the strength of electron-magnon scattering with increasing H, leading to the H dependence of C_{em} in Fig. 5(c).

We further notice that the natural oxidation process would introduce impurities into FGT, leading to additional considerable EEI. In experiments, we bake FGT nanoflakes on the hot plate at 150 °C in ambient conditions to accelerate the oxidation process. Figure 6(a) shows a metal-insulator transition as the oxidation time or disorder increases. The sheet resistance R_{xx} at low temperatures also obeys the $T^{1/2}$ law, implying the contributions of EEI and/or weak localization [35,36]. Moreover, the sheet resistance is enhanced after the oxidation process. The normalized $R_{xx}/R_{xx,p}$ at room temperature, with $R_{xx,p}$ being the sheet resistivity of the pristine sample, increases with increasing oxidation time of FGT. Figure 6(b) shows that, for thick FGT nanoflakes, A_{AH}/A_R initially increases from 2.0 to 2.6 when $R_{xx}/R_{xx,p}$ increases with increasing oxidation time, and then it remains nearly constant as the oxidation time further increases. Similarly, for thin pristine FGT nanoflakes, the A_{AH}/A_R is still >2.0 before the oxidation process. Since the value of A_{AH}/A_R deviates from the ideal value of 2.0 for the EEI mechanism, other effects, such as the weak localization effect and an orbital two-channel Kondo effect, should be considered [40,44,45]. Additionally, exchange bias has been observed in the FGT, possibly indicating the formation of the antiferromagnetic phase after oxidation [46]. Indeed, in the present experiments, the exchange field of 500 Oe is observed in 13-nm-thick oxidized FGT nanoflakes at low temperatures. Therefore, the anomalies of the sheet resistivity and the AHE in oxidized FGT needs further experimental and theoretical investigation.

IV. CONCLUSION

In summary, in this paper, we demonstrate the scaling relation of the AHE in vdW ferromagnet FGT. The scaling relation is found to be $\sigma_{\mathrm{AH}} \propto \sigma_{xx}^{\gamma}$ by varying the FGT nanoflake thickness, where $\gamma = 1.4$–2.2 as temperature changes from 2 K to its Curie temperature of 200 K. The observed scaling behavior falls within the cross-region between the intrinsic and dirty regimes, suggesting the contribution of the AHE from the intrinsic Berry curvature and the strong scattering. The low conductivity of FGT, near the dirty regime, is attributed to the heavy fermion characteristics and disorder scattering induced by Fe vacancies. These strong scattering events in FGT lead to a suppression of the intrinsic Berry curvature [32]. Moreover, the observed low-temperature anomalies of ρ_{xx} and ρ_{AH} are interpreted as the quantum correction of 3D-enhanced EEI due to Fe vacancies. Further introduced disorder by oxidation also induces weak localization into the system, in addition to the EEI, resulting in nonzero quantum correction to σ_{AH}. In light of complex physics in FGT, in this paper, we provide a clear scaling relation of the AHE, which may help us to understand electrical transport properties of other vdW ferromagnets.

ACKNOWLEDGMENT

This paper was supported by the National Key Research and Development Program of China (Grant No. 2022YFA1204002) and the National Natural Science Foundation of China (Grant No. 12274323).

---

[1] A. K. Geim and I. V. Grigorieva, Nature (London) **499**, 419 (2013).

[2] K. S. Novoselov, A. Mishchenko, A. Carvalho, and A. H. Castro Neto, Science **353**, aac9439 (2016).

[3] K. S. Novoselov, A. K. Geim, S. V. Morozov, D. Jiang, Y. Zhang, S. V. Dubonos, I. V. Grigorieva, and A. A. Firsov, Science **306**, 666 (2004).

[4] A. Avsar, H. Ochoa, F. Guinea, B. Özyilmaz, B. J. van Wees, and I. J. Vera-Marun, Rev. Mod. Phys. **92**, 021003 (2020).

[5] N. Mounet, M. Gibertini, P. Schwaller, D. Campi, A. Merkys, A. Marrazzo, T. Sohier, I. E. Castelli, A. Cepellotti, G. Pizzi *et al.*, Nat. Nanotechnol. **13**, 246 (2018).

[6] X. Lin, W. Yang, K. L. Wang, and W. Zhao, Nat. Electron. **2**, 274 (2019).

[7] N. D. Mermin and H. Wagner, Phys. Rev. Lett. **17**, 1133 (1966).

[8] B. Huang, G. Clark, E. Navarro-Moratalla, D. R. Klein, R. Cheng, K. L. Seyler, D. Zhong, E. Schmidgall, M. A. McGuire, D. H. Cobden *et al.*, Nature (London) **546**, 270 (2017).

[9] C. Gong, L. Li, Z. Li, H. Ji, A. Stern, Y. Xia, T. Cao, W. Bao, C. Z. Wang, Y. Wang *et al.*, Nature (London) **546**, 265 (2017).

[10] Y. J. Deng, Y. J. Yu, Y. C. Song, J. Z. Zhang, N. Z. Wang, Z. Y. Sun, Y. F. Yi, Y. Z. Wu, S. W. Wu, J. Y. Zhu *et al.*, Nature (London) **563**, 94 (2018).

[11] J. Seo, D. Y. Kim, E. S. An, K. Kim, G.-Y. Kim, S.-Y. Hwang, D. W. Kim, B. G. Jang, H. Kim, G. Eom *et al.*, Sci. Adv. **6**, eaay8912 (2020).

[12] G. Zhang, F. Guo, H. Wu, X. Wen, L. Yang, W. Jin, W. Zhang, and H. Chang, Nat. Commun. **13**, 5067 (2022).

[13] C. Tan, J. Lee, S. G. Jung, T. Park, S. Albarakati, J. Partridge, M. R. Field, D. G. McCulloch, L. Wang, and C. Lee, Nat. Commun. **9**, 1554 (2018).

[14] Y. Zhang, H. Lu, X. Zhu, S. Tan, W. Feng, Q. Liu, W. Zhang, Q. Chen, Y. Liu, X. Luo *et al.*, Sci. Adv. **4**, eaao6791 (2018).

[15] K. Kim, J. Seo, E. Lee, K. T. Ko, B. Kim, B. G. Jang, J. M. Ok, J. Lee, Y. J. Jo, W. Kang *et al.*, Nat. Mater. **17**, 794 (2018).

[16] S. Onoda, N. Sugimoto, and N. Nagaosa, Phys. Rev. Lett. **97**, 126602 (2006).

[17] N. Nagaosa, J. Sinova, S. Onoda, A. H. MacDonald, and N. P. Ong, Rev. Mod. Phys. **82**, 1539 (2010).

[18] S. Onoda, N. Sugimoto, and N. Nagaosa, Phys. Rev. B **77**, 165103 (2008).

[19] A. Langenfeld and P. Wölfle, Phys. Rev. Lett. **67**, 739 (1991).

[20] Y. M. Lu, J. W. Cai, Z. Guo, and X. X. Zhang, Phys. Rev. B **87**, 094405 (2013).

[21] L. Wu, K. Zhu, D. Yue, Y. Tian, and X. Jin, Phys. Rev. B **93**, 214418 (2016).

[22] Y. M. Xiong, P. W. Adams, and G. Catelani, Phys. Rev. Lett. **104**, 076806 (2010).

[23] H. Siddiquee, C. Broyles, E. Kotta, S. Liu, S. Peng, T. Kong, B. Kang, Q. Zhu, Y. Lee, L. Ke *et al.*, Nat. Commun. **14**, 527 (2023).

[24] M. Huang, S. Wang, Z. Wang, P. Liu, J. Xiang, C. Feng, X. Wang, Z. Zhang, Z. Wen, H. Xu *et al.*, ACS Nano **15**, 9759 (2021).

[25] Y. D. Sun, J. Zhang, T. Y. Yao, X. F. Sun, S. H. Ke, J. L. Zhang, and S. M. Zhou, Phys. Rev. B **107**, 094416 (2023).

[26] H. J. Deiseroth, K. Aleksandrov, C. Reiner, L. Kienle, and R. K. Kremer, Eur. J. Inorg. Chem. **2006**, 1561 (2006).

[27] H. L. Zhuang, P. R. C. Kent, and R. G. Hennig, Phys. Rev. B **93**, 134407 (2016).

[28] F. Lacy, Nanoscale Res. Lett. **6**, 636 (2011).

[29] R. Roemer, C. Liu, and K. Zou, npj 2D Mater. Appl. **4**, 33 (2020).

[30] T. Miyasato, N. Abe, T. Fujii, A. Asamitsu, S. Onoda, Y. Onose, N. Nagaosa, and Y. Tokura, Phys. Rev. Lett. **99**, 086602 (2007).

[31] X. Q. Lin and J. Ni, Phys. Rev. B **100**, 085403 (2019).

[32] G. K. Shukla, A. K. Jena, N. Shahi, K. K. Dubey, I. Rajput, S. Baral, K. Yadav, K. Mukherjee, A. Lakhani, K. Carva *et al.*, Phys. Rev. B **105**, 035124 (2022).

[33] J. Kondo, Prog. Theor. Phys. **32**, 37 (1964).

[34] H. T. Liu, Y. Z. Xue, J. A. Shi, R. A Guzman, P. P. Zhang, Z. Zhou, Y. G. He, C. Bian, L. M. Wu, R. S. Ma *et al.*, Nano Lett. **19**, 8572 (2019).

[35] G. Bergmann, Phys. Rep. **107**, 1 (1984).

[36] B. L. Altshuler and A. G. Aronov, in *Electron-Electron Interactions in Disordered Systems*, edited by A. L. Efros and M. Pollak (North-Holland, Amsterdam, 1985).

[37] P. Mitra, R. Misra, A. F. Hebard, K. A. Muttalib, and P. Wölfle, Phys. Rev. Lett. **99**, 046804 (2007).

[38] G. Bergmann and F. Ye, Phys. Rev. Lett. **67**, 735 (1991).

[39] K. A. Muttalib and P. Wölfle, Phys. Rev. B **76**, 214415 (2007).

[40] V. K. Dugaev, A. Crépieux, and P. Bruno, Phys. Rev. B **64**, 104411 (2001).

[41] S. Tong, X. Zhao, D. Wei, and J. Zhao, Phys. Rev. B **101**, 184434 (2020).

[42] I. Mannari, Prog. Theor. Phys. **22**, 335 (1959).

[43] W. Ma, X. Zhang, and K. Takahashi, J. Phys. D **43**, 465301 (2010).

[44] H. Feng, Y. Li, Y. Shi, H. Xie, Y. Li, and Y. Xu, Chin. Phys. Lett. **39**, 077501 (2022).

[45] L. J. Zhu, S. H. Nie, P. Xiong, P. Schlottmann, and J. H. Zhao, Nat. Commun. **7**, 10817 (2016).

[46] H. K. Gweon, S. Y. Lee, H. Y. Kwon, J. Jeong, H. J. Chang, K. W. Kim, Z. Q. Qiu, H. J. Ryu, C. Jang, and J. W. Choi, Nano Lett. **21**, 1672 (2021).